HHS Public Access

Author manuscript

Science. Author manuscript; available in PMC 2016 March 29.

Published in final edited form as:

Science. 2015 November 27; 350(6264): aac9462. doi:10.1126/science.aac9462.

Principles of connectivity among morphologically defined cell types in adult neocortex

Xiaolong Jiang[1,*], **Shan Shen**[1], **Cathryn R. Cadwell**[1], **Philipp Berens**[1,2,3,4], **Fabian Sinz**[1], **Alexander S. Ecker**[1,2,4,5], **Saumil Patel**[1], and **Andreas S. Tolias**[1,2,*]

[1]Department of Neuroscience, Baylor College of Medicine, Houston, TX, USA

[2]Bernstein Centre for Computational, Neuroscience, Tübingen, Germany

[3]Institute for Ophthalmic Research University of Tübingen, Tübingen, Germany

[4]Werner Reichardt Center for Integrative Neuroscience and Institute of Theoretical Physics, University of Tübingen, Tübingen, Germany

[5]Max Planck Institute for Biological Cybernetics, Tübingen, Germany

Abstract

Introduction—The intricate microcircuitry of the cerebral cortex is thought to be a critical substrate from which arise the impressive capabilities of the mammalian brain. Until now, our knowledge of the stereotypical connectivity in neocortical microcircuits has been pieced together from individual studies of the connectivity between small numbers of neuronal cell types. Here, we provide unbiased, large-scale profiling of neuronal cell types and connections to reveal the essential building blocks of the cortex and the principles governing their assembly into cortical circuits. Using advanced techniques for tissue slicing, multiple simultaneous whole-cell recording, and morphological reconstruction, we are able to provide a comprehensive view of the connectivity between diverse types of neurons, particularly among types of γ-aminobutyric acid–releasing (GABAergic) interneurons, in the adult animal.

Rationale—We took advantage of a method for preparing high-quality slices of adult tissue and combined this technique with octuple simultaneous, whole-cell recordings followed by an improved staining method that allowed detailed recovery of axonal and dendritic arbor morphology. These data allowed us to perform a census of morphologically and electrophysiologically defined neuronal types (primarily GABAergic interneurons) in neocortical layers 1, 2/3, and 5 (L1, L23, and L5, respectively) and to observe their connectivity patterns in adult animals.

Results—Our large-scale, comprehensive profiling of neocortical neurons differentiated 15 major types of interneurons, in addition to two lamina-defined types of pyramidal neurons (L23 and L5). Cortical interneurons comprise two types in L1 (eNGC and SBC-like), seven in L23 (L23MC, L23NGC, BTC, BPC, DBC, L23BC, and ChC), and six in L5 (L5MC, L5NGC, L5BC, SC, HEC, and DC) (see the figure). Each type has stereotypical electrophysiological properties

Corresponding author. astolias@bcm.edu (A.S.T.); xiaolonj@bcm.edu (X.J.).

Supplementary Materials: www.sciencemag.org/content/350/6264/aac9462/suppl/DC1

and morphological features and can be differentiated from all others by cell type-specific axonal geometry and axonal projection patterns. Importantly, each type of neuron has its own characteristic input-output connectivity profile, connecting with other constituent neuronal types with varying degrees of specificity in postsynaptic targets, laminar location, and synaptic characteristics. Despite specific connection patterns for each cell type, we found that a small number of simple connectivity motifs are repeated across layers and cell types defining a canonical cortical microcircuit.

Conclusion—Our comprehensive profiling of neuronal cell types and connections in adult neocortex provides the most complete wiring diagram of neocortical microcircuits to date. Compared with current genetic labels for cell class, which paint the cortex in broad strokes, our analysis of morphological and electrophysiological properties revealed new cell classes and allowed us to derive a small number of simple connectivity rules that were repeated across layers and cell types. This detailed blueprint of cortical wiring should aid efforts to identify specific circuit abnormalities in animal models of brain disease and may eventually provide a path toward the development of comprehensive circuit-based, cell type-specific interventions.

Graphical abstract

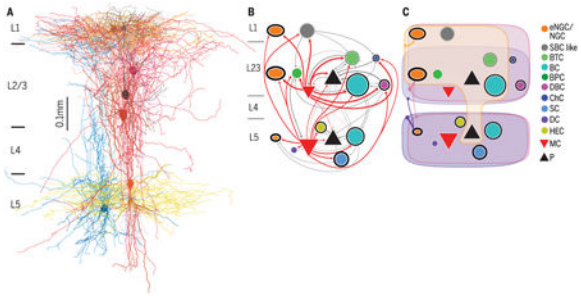

Connectivity among morphologically defined cell types in adult neocortex. (**A**) Simultaneous octuple whole-cell recording to study connectivity followed by morphological reconstruction. (**B**) Synaptic connectivity between morphologically distinct types of neurons, including pyramidal (P) neurons. (**C**) Connectivity from neurogliaform cells (NGCs) to other cell types. This connectivity is believed to be nonsynaptic and mediated by volume transmission. Martinotti cell, MC; basket cell, BC; single-bouquet celllike cell, SBC-like; bitufted cell, BTC; bipolar cell, BPC, double-bouquet cell, DBC; chandelier cell, ChC; shrub cell, SC; horizontally elongated cell, HEC; deep-projecting cell, DC.

Despite its importance, we are still far from completely understanding the extensive diversity of cell types in the neocortex and how they are connected into functional circuits. Neocortical neurons fall into two broad classes. Excitatory glutamatergic neurons form the majority and exhibit relatively stereotypical properties, whereas inhibitory γ-aminobutyric acid-releasing (GABAergic) interneurons are highly diverse (1). GABAergic interneurons show many distinct morphological, electrophysiological, neurochemical, and synaptic wiring features (1–6). Due to the complex and multifaceted nature of interneurons, there is still no consensus on how many types of interneurons exist in the neocortex, and unequivocal identification of the features that distinguish one type of neuron from another is a matter of considerable interest and debate (2, 4). Maturation of GABAergic interneurons

takes longer than for pyramidal cells, and their continuous development throughout adolescence into adulthood often further obscures our understanding (7, 8). Therefore, it is imperative to study the mature neocortex to gain a true understanding of interneuron cell types in the neocortex. However, the vast majority of in vitro slice electrophysiology experiments to date were carried out in juvenile animals due to the technical difficulties of preparing high-quality slices from adult tissue.

Morphologically defined interneuron types in neocortex

We took advantage of a recently developed adult animal slicing method (9) to study mature neocortical circuitry. We performed simultaneous octuple whole-cell recordings in acute slices prepared from the primary visual cortex (area V1) of adult mice (≥2 months old) and focused on neurons from layers 1, 2/3, and 5 (L1, L23, and L5, respectively) because these layers are particularly enriched with GABAergic interneurons (10). We recorded both GABAergic neurons (n = 1654) and pyramidal neurons (n = 547) to identify their connections, followed by post hoc morphological recovery of each neuron with an optimized avidinbiotin-peroxidase staining method (fig. S1 and supplementary materials). Using this technique, we recovered the morphology of all recorded pyramidal neurons (n = 547/547,100%), and almost all recorded GABAergic interneurons (n = 1566/1654, ≥95%), especially their fine axonal arbors (fig. S1A).

The morphologies of interneurons were highly diverse, whereas the morphologies of pyramidal neurons in L23 and L5 were relatively uniform (for a discussion of the morphological diversity of pyramidal cells, see the supplementary text). Morphologically recovered interneurons were visually assessed or reconstructed if necessary under microscopy and then were classified following a widely used classification scheme based on their axonal geometry (thickness, tortuosity, bifurcation angle, branching order, and the shape of terminal branches) and their axonal projection pattern (1, 4, 5). We could differentiate recorded interneurons into 15 major types: two types in L1, seven in L23, and six in L5 (Fig. 1, A to C). To quantitatively support our classification, a subset of neurons from each type were fully reconstructed to carry out dendritic and axonal length density analysis (figs. S2 and S3) (n = 24 in L1, n = 96 in L23, and n = 73 in L5). We extracted simple features from the axon and dendrite density maps of the reconstructed neurons using principal component analysis (11) and trained cross-validated sparse logistic regression classifiers to distinguish between any two types of interneurons as labeled manually (see the supplementary materials). The classifiers could separate almost all cell type pairs with an accuracy of >90% and an average performance of ∼97%, supporting the notion that our 15 classes represent distinct types (Fig. 1D). The classifiers mostly used features computed from the axon density map, giving support to the idea that interneurons can primarily be distinguished based on their axonal features (fig. S4).

Two types of layer 1 interneurons

The neurons recorded in L1 of mature V1 could be morphologically divided into two major types, which were generally similar to those described in juvenile animals (5, 12). One type of neuron was neurogliaform cells (NGCs, n = 84) with elongated axonal arborization (Figs. 1A and 3A and figs. S2A, S2D, S5A, S6B, and S7). We follow the previous nomenclature

naming them elongated NGCs (eNGC). The vast majority of eNGCs (n = 77/84 neurons) fired late-spiking (LS) action potentials (APs) followed by a deep, wide after hyperpolarization (AHP) (Fig. 2A, Type 1, and table S1). The eNGCs constituted about one-third of all L1 neurons (Fig. 1E). The remaining L1 neurons had axonal projection patterns (Figs. 1A and 3A and figs. S2A, S5A, S6B, and S7), dendritic features (fig. S3, A and D), and electrophysiological properties (Fig. 2A and tables S1 and S2) that were clearly distinct from eNGCs. Some of them (~40%) had an axon that was very similar to single-bouquet cells (SBCs) reported in juvenile rat somatosensory cortex (5, 12). However, many of them (~60%) had atypical axonal projection patterns compared to those previously described for SBCs, and their axon arborized mostly within L1, with only one or two side branches extending to deep layers (not deeper than L4). Despite their variable axonal projection patterns, non-neurogliaform L1 neurons shared similar dendritic and electrophysiological features (tables S1 and S2) and similar connectivity profiles (table S3) that correspond to SBCs in rat somatosensory cortex (5, 12). We thus refer to this group as SBC-like cells. A detailed description of the morphology, firing patterns, and intrinsic membrane properties of these two major types of L1 neurons can be found in the supplementary text.

Seven types of layers 2/3 interneurons

Interneurons from L23 of mature V1 could be grouped into seven major types based on axonal morphology (Fig. 1, B and C): L23 Martinotti cells (L23MCs, n = 182), L23 neurogliaform cells (L23NGCs, n = 102), bitufted cells (BTCs, n = 118), bipolar cells (BPCs, n = 85), double bouquet cells (DBCs, n = 46), L23 basket cells (L23BCs, n = 322), and chandelier cells (ChCs, n = 18). All of these L23 neuronal types have been previously reported in juvenile rodents (1, 5, 13, 14). (For a detailed description of their axonal and dendritic morphology, see the supplementary text). For some of these types (for instance, BPC and BC), the morphology in mature neocortex did not completely match the morphological description for this cell type in the developing neocortex, which could be due to differences in either age or species (mouse versus rat; see the supplementary text). Each type of L23 interneuron had a characteristic axonal projection pattern (Fig. 1, B and C), which was confirmed by axonal length density analysis and pairwise type classification (Fig. 1D and figs. S2, B and E, and S4). Neurons within a type tended to have the same dendritic arborization patterns (see the supplementary text), but these patterns were often not type-specific (figs. S3, B and E, and S4). The morphological types varied greatly in population size, with L23BCs being the largest population of L23 interneurons (40%) and ChC being the smallest (2%) (Fig. 1E).

Firing patterns and intrinsic membrane properties of L23 interneurons were mostly stereotypical within a cell type (see the supplementary text) but again were often not cell type-specific (Fig. 2B and table S1). For instance, L23BCs and ChCs were both fast-spiking (FS), consistent with previous observations. All DBCs in mature V1 were FS, which had not been previously reported (Fig. 2B and table S1). All BPCs exhibited an irregular spiking pattern with or without initial burst (Fig. 2B), and this irregular spiking pattern was also seen in a large proportion of BTCs (Fig. 2B). BTCs exhibited the most diverse firing patterns, and some of them had a firing pattern similar to MCs (Fig. 2B). Nevertheless, L23MCs and L23NGCs appeared to have firing patterns and intrinsic membrane properties that were

mostly cell type-specific and could be used to differentiate them from most of the other neuronal cell types (except for a small number of BTCs) (see Fig. 2B).

Six types of layer 5 interneurons

Interneurons in L5 of mature V1 could be grouped into six major types based on their axonal morphology, only one of which had been reported and characterized before in the developing neocortex (Martinotti cells; L5MCs) (15, 16). The remaining five types have not been previously described in L5, and we named them as follows: neurogliaform cells (L5NGCs), basket cells (L5BCs), shrub cells (SCs), horizontally elongated cells (HECs), and deep-projecting cells (DCs) (Fig. 1, B and C). Each of these types had a characteristic axonal projection pattern (Fig. 1, B to D, and fig. S4), which was confirmed by axonal length density analysis and pairwise type classification (Fig. 1D and figs. S2, C and F, and S4). Neurons within a type also tended to have the same dendritic arborization pattern and electrophysiological properties, but as for L23 interneurons, these properties were often not cell type–specific (figs. S3, C and F, and S4). L5 morphological types also varied greatly in population size, with L5BCs and L5MCs being the largest population of L5 interneurons (32%) and L5NGCs being the smallest (3%) (Fig. 1E). Because most of these L5 interneuron types have not been previously reported, we describe the morphology and electrophysiology of each type in detail below.

L5 Martinotti cell—L5MCs in mature neocortex (n = 174) were very similar to L5MCs previously reported in the developing neocortex (15, 16). The majority of L5MCs had bitufted somatodendritic morphology with an elaborate dendritic tree that ascended and descended toward L23 and L6, respectively (Figs. 1B and 3A; and figs. S3, C and F; S5, A and D; S7; S8B; fig. S9, D and E; and fig. S10A), and a small number of L5MCs from deeper L5 (L5B) had multipolar somatodendritic morphology (Figs. 1B and 3, A and B, and fig. S7). The axons of L5MC originated from the pia side of the somata or one of the primary dendrites, then ascended to form large axonal clusters in L1 and L4 (or, less often, in L1 and L5) (Figs. 1B and 3, A and B; and figs. S2, C and F; S5, A and D; S7; S8B, S9, D and E; and S10A). All L5MCs exhibited a firing pattern similar to their young counterparts (13, 16, 17) except that they could not sustain continuous firing in response to prolonged current injection (Fig. 2C and table S1). About one-fourth of L5MCs could generate a rebound burst after cessation of the hyperpolarization step (Fig. 2C, Type 1, 44/164), reminiscent of low-threshold-spiking interneurons in the developing neocortex (16, 17). The remaining three-fourths of L5MCs did not exhibit a rebound burst (Type 2, 120/164). In addition, L5MC, similar to L23MCs, had a characteristic intrinsic membrane property: All L5MCs had a very large membrane time constant (table S1).

L5 neurogliaform cell—We called this L5 cell type neurogliaform cells (L5NGC, n = 17) because they had axonal and dendritic geometry typical of NGCs in other layers. However, their axonal arborization was vertically elongated, different from NGCs in L1 and L23 (Figs. 1B and 3C and figs. S2, C and F, and S7). All L5NGCs had a late-spiking firing pattern, similar to the firing patterns of NGCs in L1 (Type 1) and L23 (Figs. 2C and table S1).

L5 basket cell—We called this L5 cell type basket cells (L5BC, *n* = 151) based on their similarity to L23BCs (see the supplementary text). They had a roughly vertically oriented, bitufted-like dendritic tree (Figs. 1C and 3B; and figs. S3, C and F; S5, B to D; S7; S9B, and S10, A and B) and a thick axon that typically originated from the apical side of the somata and ascended into L23 but never extended into L1 (Figs. 1C and 3B; and figs. S2, C and F; S5, B to D;S7; S9B; and S10, A and B). All L5BCs were FS (Fig. 2C and table S1).

Shrub cell

This type of interneuron in L5 was named based on the shrub-like axonal field that they exhibited (SC, *n* = 77). These cells had a characteristic asymmetric dendritic tree, with most of the dendritic branches localized above the somata (Figs. 1C and 3C; and figs. S3, C and F; S5, A and B; S7; and S10B). The axon typically originated from the apical side of the somata and ascended for a short distance before bifurcating into several main branches that then arborized into a short shrub-like axonal field above the somata (Figs. 1C and 3C; and figs. S2,C and F;S5, A and B; S7; and S10B). All SCs were FS (Fig. 2C and table S1).

Horizontally elongated cell

This type was named based on the horizontally elongated axonal arbors (HEC, *n* = 54). HECs had a multipolar somatodendritic morphology (Fig. 3A and figs. S3, C and F and S5C) and a thick axon that originated from either the base or the apical side of the somata and arborized into a narrow, horizontally elongated axonal field (Figs. 1B and 3A; and figs. S2, C and F; S5C; S7; and S10B). The vast majority of HECs (53/54) had a FS firing pattern (Fig. 2C and table S1).

Deep-projecting cell

This cell type had a multipolar somatodendritic morphology (fig. S3, C and F), and their axons primarily descended toward deeper cortical areas, even to layer 6 (Figs. 1B and 3C; and figs. S2, C and F, and S7). Therefore, we refer to them as deep-projecting cells (DCs; *n* = 27). Although all DCs discharged irregularly, their firing patterns could be differentiated into two types with subtle differences [Type 1,15/22, with after depolarization (ADP); and Type 2, a deeper and faster AHP and no ADP, 7/22] (Fig. 2C and table S1).

Overlap of morphological types with Cre driver lines

In many experiments, we used Viaat-Cre/Ai9 mice (*n* = 81) to facilitate targeting of GABAergic interneurons (18). All unlabeled neurons recorded from L23 (*n* = 120) and L5 (*n* = 105) in these transgenic mice were morphologically and electrophysiologically confirmed as pyramidal neurons, and none were interneurons, suggesting that indeed the entire population of GABAergic interneurons in L23 and L5 was labeled in these mice. Almost all labeled neurons in L23 were morphologically confirmed as interneurons with distinct morphology (401/402) (table S4). The vast majority of labeled neurons in L5 were also confirmed as interneurons (269/289), although a small percentage (∼7%, 20/289) were pyramidal neurons (table S4). In contrast to L23 and L5, a considerable proportion of L1 interneurons were unlabeled (∼26%, *n* = 25/95), and, interestingly, all unlabeled interneurons were SBC-like cells.

Several Cre lines label subpopulations of interneurons. To determine the morphological cell types labeled by specific Cre driver lines, we recovered the morphology of parvalbumin-expressing (PV^+), somatostatin-expressing (SOM^+) and vasointenstinal peptide-expressing (VIP^+) interneurons using PV-Cre/Ai9 (n = 18 mice), SOM-Cre/Ai9 (n = 30 mice), and VIP-Cre/Ai9 (n = 5 mice) transgenic mice, respectively. The vast majority of recovered PV^+ neurons in L23 were BCs (n = 80/82) (fig. S10B and table S4), and only two were ChCs. In L5, most recovered PV^+ neurons were BCs as well (60%, 26/43) (fig. S10B and table S4), and the rest were either SCs (23%, n = 10/43) (fig. S10B) or HECs (19%, n = 8/43) (fig. S10B and table S4). Most recovered SOM^+ neurons in both L23 and L5 were MCs (~70%, 133/190) (fig. S10A and table S4), consistent with the long-held contention that all MCs express somatostatin (13). However, some SOM^+ neurons were fast spiking and had a morphology corresponding to BCs (21.5%, 41/190) (fig. S10A and table S4) (1, 19, 20), indicating that some BCs were labeled in SOM-transgenic mice. In addition, a few SOM^+ neurons in L23 had a morphology corresponding to BTCs (n = 10/100, 10%) (fig. S10A and table S4), consistent with previous observations that some BTCs express SOM (1). The VIP^+ neurons in L23 were either BTCs (55%, 22/40) or BPCs (45%, 18/40), consistent with previous reports (fig. S10B and table S4) (1, 21, 22). VIP^+ neurons in L5 were very sparse, and we did not successfully recover any L5 VIP^+ neurons.

The overlap of morphological types with Cre driver lines suggested that specific genetic markers are expressed in some morphologically defined interneuron type (table S5). Some of the morphologically defined interneuron types could be recovered from two lines (for instance, BTC and BC), whereas some types were not found in any of the PV^+, SOM^+, or VIP^+ Cre driver lines (table S5). Specifically, all DBCs exhibited a FS firing pattern, suggesting that they might be PV^+. However, we did not recover any DBCs from PV^+ interneurons. Similarly, the firing pattern of DCs suggested that they may express VIP (23, 24), but we did not recover any DCs from VIP^+ interneurons. Finally, L1 interneurons and all NGCs across the layers could not be recovered from any of the three Cre driver lines (table S5), underscoring the importance of identifying specific molecular markers for these cell types.

Principles of connectivity in neocortical microcircuit

Synaptic connections were identified by evoking unitary excitatory or inhibitory postsynaptic potentials [uE(I)PSPs] on postsynaptic neurons with brief depolarizing current pulses applied in pre-synaptic neurons (fig. S1B). We identified a total of 1680 connections (both inhibitory and excitatory) from 11,771 putative connections tested between 175 L1, 1139 L23, and 782 L5 morphologically identified neurons (Fig. 3). For inhibitory connections, the latencies of uIPSPs were typically less than 2 ms (1.84 ± 0.3 ms, n = 1020) unless the presynaptic neuron was a neuroglia-form cell (latency: 4.74 ± 0.13 ms, n = 275) (fig. S11A) (5, 25). The short latency of u(E)IPSPs and the response of the uIPSP latency to glutaminergic antagonists suggested that all identified connections were monosynaptic (fig. S11, B and C and supplementary materials).

Because interneurons generally have localized axonal arbors, their interactions with other neurons should depend on the distance between neurons. We thus computed the inhibitory

connection probability as a function of intersoma Euclidean, horizontal (X) or vertical (Y) distance for all pairs (figs. S1A and S12A). Connection probability decreased sharply with distance ($P < 0.02$; Kruskal–Wallis test), leveling off after ~250 μm but not quite reaching zero, primarily due to vertical connections between cells in different cortical layers (fig. S12, A and B). The connectivity dropped more quickly in the horizontal plane than in the vertical (fig. S12A), indicating that the inhibition from an inter-neuron was more far-reaching in the vertical than in the horizontal direction. The connectivity was higher between L23 neurons than between L5 neurons (fig. S12B). Because intersomatic distance is an important factor determining the connectivity, only within-layer pairs with a Euclidean distance < 250 μm and across-layer pairs with a horizontal distance < 150 μm were included in the subsequent connectivity analysis (figs. S12, A to C, and S13).

Next, we examined the connectivity at the level of the morphologically defined cell types (both interneurons and pyramidal cells) (Figs. 3 and 4A, fig. S14, and supplementary text). The connectivity of each type was not random, but highly predictable, and each morphologically distinct type of neuron had its own characteristic input-output connectivity profile, connecting with other constituent neuronal types with varying degrees of specificity in postsynaptic targets, layer location, and synaptic characteristics (Figs. 3 and 4A and fig. S14) (see the supplementary text for a detailed description). The probability of a connection between two specific types of neurons strongly correlated with their average synaptic connection strength (Fig. 5A), and this correlation applied to all types of connections, including interneuron→interneuron, interneuron→pyramidal neuron, and pyramidal neuron→interneuron connections (Fig. 5A and table S6).

Three major groups of interneurons with distinct output connection rules

Although each type of interneuron had a specific output connectivity profile, the 15 morphologically distinct interneuron types generally followed three output connection rules and thus could be divided into three major groups. The first group consisted of interneurons that appeared to project nonspecifically to almost all neuronal types within the home layer and some of them even to almost all neuronal types across several layers (for instance, L5MCs). Because of this connection pattern, we call this group “master regulators.” It includes NGCs and MCs in different layers (Figs. 4A and 6, A and B; fig. S14; and supplementary text). The second group consisted of interneuron types that only projected to other interneurons and not to pyramidal cells, and we refer to them as interneuron-selective interneurons (ISIs), which included SBC-like cell, BPCs, and DCs (Figs. 4A and 6D, fig. S14, and supplementary text). The remaining interneuron types projected to local pyramidal neurons, and we refer to them as pyramidal-neuron-targeting interneurons (PTIs), which included L23BCs, L5BCs, DBCs, ChCs, HECs, SCs, and BTCs (Figs. 4A and 6C and fig. S14). Moreover, most PTIs (L23BCs, L5BCs, DBCs, ChCs, HECs, and SCs) also preferentially projected to interneurons of the same morphological type (Figs. 4A and 6C and fig. S14). In addition to projecting to pyramidal neurons and themselves, some types of PTIs projected to certain specific types of interneuron with distinct connectivity (for instance, BTCs and BCs projected to MCs) (Figs. 4A and 6D and fig. S14). Neurons from each of these three classes (master, PTI, and ISI) could be found in each cortical layer. For instance, MCs in L23 and L5 provided a uniform inhibition to every neuronal type (except

MCs) within L23 and L5, respectively, and the layers above them (Fig. 4A and 6B and fig. S14); NGCs in L1, L23, and L5 provided a uniform inhibition to every neuronal type within L1, L23, and L5, respectively, and in the nearby layers (Fig. 4A and 6B and fig. S14). The three ISIs are equally distributed between layers and serve a disinhibitory role. Several L23 PTIs appeared to have closely matched cell types in L5 (Fig. 4A and fig. S14), and the connectivity motifs of PTIs are recycled across L23 and L5.

Two master regulators with distinct input profiles

NGCs and MCs projected to almost every neuronal type with a similar high connection probability (Figs. 4A and 6, A and B, and fig. S14), indicating that NGCs and MCs act as master regulators by providing nonspecific inhibition to the local neocortical circuit. However, NGCs and MCs have very different input connectivity profiles and output mechanisms, suggesting that these two master regulators operate in fundamentally different ways.

Within their home layer, a single AP in NGCs elicited large, slow uIPSPs in almost all simultaneously recorded neurons, regardless of their type (Fig. 3C). This was observed in NGCs from all layers (L1, L23, and L5) (Fig. 3, A and C; and figs. S5A; S6, A and B; and S14). The connection probability from NGCs reached up to 90% if postsynaptic somata were located ≤100 μm apart. This exceptionally high connectivity, the lack of postsynaptic specificity, and the unusual, slow synaptic events evoked by NGCs support the notion that NGCs use volume transmission (25, 26) (Fig. 6A). Projection patterns from L23 and L5 NGCs to nearby layers are also consistent with this idea (Figs. 4A and 6A and fig. S14). Nevertheless, L1 eNGCs exhibited a certain degree of postsynaptic specificity in projecting to L23 neurons (they preferentially project to BPC, BTC, and NGCs in L23) (Figs. 4A and 6A and fig. S14), which seems to argue against volume transmission for this cell type (27). However, because the axon of eNGCs is restricted to L1, for any L23 neuron to interact with an eNGC, it must have a dendritic tree extending into L1. The preferential projection to BPC, BTC, and NGCs thus may simply reflect that more of their dendritic trees extend into L1, making them more likely to be exposed to a cloud of GABA released there than other types of L23 interneurons. Therefore, the projection pattern from L1 eNGCs to L23 may still be consistent with the mechanism of volume transmission (Fig. 6A).

Similar to NGCs, a single spike in MCs elicited uIPSPs in all non-MC neuronal types within home layers and the layers above them (Figs. 3, A and B, and 6B; and figs. S5, A and D; S6, A and C; S8, A to C; and S9A). However, MCs differ from NGCs in several important ways. First, MCs use synaptic transmission rather than volume transmission, as evidenced by the fast kinetics of their uIPSPs (fig. S11) and their ability to selectively avoid inhibiting other MCs (Figs. 4A and 6B and fig. S14). Second, MCs received strong inputs from local pyramidal neurons with strongly facilitating synapses (15.4% and 4.5% from L23 and L5 pyramidal neurons, respectively, pooled across all MC types) (Figs. 5B and 6D and fig. S14), whereas NGCs received very little input from local pyramidal neurons, especially from L23 pyramidal neurons (0.0% and 2.1% from L23 and L5 pyramidal neurons, respectively; pooled across all NGC types) (Figs. 4A and 5B and supplementary text) [generalized linear model (GLM) with factors cell type and layer; effect of cell type: P =

0.002; layer: $P = 0.0006$; interaction: $P = 0.03$; for details of model fitting, see the supplementary materials]. In addition, MCs received very specific inhibition from local circuits: BCs projected to MCs within L23 and L5, BTCs projected to L23MCs, and BPCs projected almost exclusively to L5MCs (Figs. 4A and 6D and fig. S14), whereas NGCs received little specific inhibition from local circuits (aside from NGC and MC input, which is nonspecific) (Fig. 5B; $P < 0.0001$ compared with MC, Chi-square test). Therefore, MCs are locally controlled, in contrast to NGCs, which may be primarily controlled by long-range inputs. Although both NGCs and MCs serve as master regulators for the cortical microcircuit, the specific computational operations implemented by these two types may be fundamentally different.

Interneuron-selective interneurons are neither self-inhibitory nor locally recruited

ISIs included L1 SBC-like cells (0% connection to pyramidal neurons, 0/152), BPCs (0% connection to pyramidal neurons, 0/115), and DCs (0% connection to pyramidal neurons, 0/46) (Figs. 4A and 6D and fig. S14). Although all ISIs targeted only interneurons, the three ISIs had different preferences in postsynaptic targets: BPCs and DCs projected almost exclusively to L5MCs, whereas SBC-like cells targeted several interneuron types in L23 but avoided MCs (Figs. 4A and 6D and fig. S14). However, because the axon of DCs projects toward the deeper cortical areas, even into L6, they may additionally project to the interneurons in L6. All these types generally did not exhibit self-inhibition (Figs. 4A; 6, C and D; 5C; and fig. S14), which was seen in all PTI interneuron types. Interneuron-targeting interneurons also received very little input from local pyramidal neurons and specific inhibitory inputs, very different from other groups of interneurons (Fig. 5, C and D). ISIs thus may act primarily as disinhibitors of the local cortical microcircuit and may be primarily controlled by long-range inputs.

Pyramidal-neuron-targeting interneurons are self-inhibitory and locally recruited

PTIs (the seven types described above) connected to pyramidal neurons and to other interneurons of the same morphological type (self-inhibition) (Figs. 4A and 6C and fig. S14). For most of them (except BTCs), self-inhibition was the strongest output connection. This connectivity motif occurred not only within a layer but also across layers (L23BCs and L5 BCs preferentially connect with BCs and pyramidal neurons in both L23 and L5) (Figs. 4A and 6C and fig. S14). The connection rule shared by this group of neurons is thus very different from that of master regulators and ISIs (Figs. 4A; 5C; and 6, C and D; and fig. S14). In addition, there was a strong positive correlation between connectivity to pyramidal neurons and self-inhibition probability (Fig. 5C) [$r(11) = 0.72$; $P = 0.01$], indicating that a PTI's ability to inhibit local pyramidal neurons faces comparative competition from interneurons of the same morphological type.

Many PTI cell types not only inhibited local pyramidal neurons but also received strong excitatory inputs from these neurons via synapses that depressed upon repetitive stimulation (Figs. 4A and 6D and figs. S9F and S14). This reciprocal connectivity motif also occurred between interneurons and pyramidal neurons located in different cortical layers. For example, BCs in L23 projected to pyramidal neurons in L5, and they also received excitatory inputs from L5 pyramidal neurons; the same was true for L5BCs (Figs. 4A and

6D and fig. S14). This reciprocal connectivity motif between PTIs and pyramidal neurons is very different from ISIs. ISIs did not target local pyramidal neurons, and they also received very little inputs from local pyramidal neurons (Figs. 4A, 5D, and 6D and fig. S14). These observations indicate that local pyramidal neurons tend to recruit interneuron types that inhibit pyramidal neurons. Nevertheless, local pyramidal neurons do not necessarily recruit all interneuron types that inhibit pyramidal neurons. There were several types of PTIs, such as DBC, that did not receive innervation from pyramidal neurons.

A simple model incorporating three connectivity rules (master, ISI, and PTI) captures most of the connectivity structure

To determine whether the three connectivity rules (master, ISI, and PTI) that we observed represent general connection rules with explanatory power, we devised a series of simple models of the connectivity matrix between the reported cell types (Fig. 4B and supplementary materials). We started from a uniform model that assumes that connectivity probabilities for each type of connections are equal (1 parameter). Then we gradually added details (layer identity, inhibitory or excitatory cell types, and the three principles) into the model, obtaining a series of models. We compared the likelihoods of these models with that of the full model, which has an individual connection probability parameter for each type of connections (289 parameters) (Fig. 4B). We wanted to see under what restrictions the model would still recapitulate the essential connectivity structure of the full model. When incorporating the three connectivity rules (master, ISI, and PTI), the model came within one bit of the performance of the full model with only about a fourth of the degrees of freedom ($d = 67$) (Fig. 4B), indicating that the identified rules captured the essential connectivity structure among the types of neurons.

Comparison to connectivity of juvenile cell types

Connectivity patterns of three molecularly identified interneuronal types (PV^+, SOM^+, and VIP^+) in the developing neocortex have been recently revealed by optogenetic studies (28–30). Although these studies are informative about the broad pattern of connections between molecularly identified interneuronal types within a layer in the developing neocortex, they are unable to capture the full functional diversity of interneurons, given that interneurons labeled in the same Cre line (PV-Cre, VIP-Cre, and SOM-Cre) in mature cortex had distinct morphologies (fig. S10, A and B, and tables S4 and S5), and the morphologically distinct interneurons from the same Cre lines had different connectivity profiles within and across layers (fig. S10C and tables S7to S9). For instance, the L5 PV^+ neurons could be morphologically classified into L5BCs, SCs, and HECs (fig. S10B), and L5BCs, SCs, and HECs, regardless of the mouse lines that they were recovered from, are FS (Fig. 2C). In addition, the connectivity of L5BCs, SCs, and HECs from different mouse lines (Viatt/ai9 and wild-type) was very similar to the connectivity of the corresponding cell types in the PV^+ Cre line (fig. S10C and table S7). All these observations strongly suggested that all L5BCs, SCs, and HECs express PV, but these L5 PV-expressing neurons do not have the same connectivity profiles within and across the layers (Fig. 4A and fig. S14). In addition, it has been increasingly recognized that the SOM-Cre driver line (SOM-IRES-Cre) (31) labels a population of neurons that can be grouped into distinct types both functionally (19, 32) and

morphologically (fig. S10A and tables S3 and S4) (20). In contrast to what has been reported in optogenetic studies [SOM$^+$ neurons avoid each other (28)], there is a high connectivity between SOM$^+$ MCs and SOM$^+$ non-MCs. Within the SOM$^+$ class, only MCs avoid connecting to each other (table S8). Moreover, several morphologically defined types could be labeled in several Cre lines (tables S4 and S5), but the connectivity patterns of the same morphological types from different lines appeared to be very similar. For instance, BTCs could be labeled in both VIP-Cre and SOM-Cre lines, and we did not observe any morphological differences between VIP$^+$ BTC and SOM$^+$ BTC (fig. S10, A and B). Although differences in other neuronal features may exist between them, they appeared to have very similar connectivity profiles (they both connected to pyramidal neurons and MCs and received input from pyramidal neurons) (tables S8 and S9 and fig. S10C). These observations provide another line of evidence that the axonal morphology of an interneuron indeed determines its connection rule.

In addition to the above-mentioned discrepancies, we noticed that several connection patterns we observed in mature neocortex appeared to be different from that in the developing neocortex. First, NGCs received very little input from local excitatory neurons (33). However, in the developing somatosensory cortex, NGCs receive excitatory inputs from L23 (34, 35). Second, there is a fair connection probability from BCs to MCs in both L23 and L5 (Figs. 4 and 6C and fig. S14), indicating that PV$^+$ cells do project to SOM$^+$ cells in mature neocortex, in contrast to a study performed in the developing neocortex (28). Third, inhibitory projections to pyramidal neurons in mature neocortex appeared to be different from the developing neocortex. In this study, we did not identify any connection from BPCs to L23 or L5 pyramidal neurons or from BTCs to L5 pyramidal neurons (Figs. 4 and 6C and fig. S14), but these types of connections have been frequently identified in the developing neocortex (5). Finally, the connectivity among mature pyramidal neurons, particularly among L5 pyramidal neurons, was much lower than the connectivity among pyramidal neurons within the same range of intersoma distance in juvenile slices [figs. S13B (average, 91 ± 4μm) and S14 and supplementary text] (36, 37). Although other experimental differences might explain some of these discrepancies (e.g., methods, cortical area, species, and low connection probability), the most compelling and consistent difference across experiments is the age of the animals tested, suggesting that mature cortical circuits are not identical to developing circuits.

Conclusions

Establishing a complete census of cell types in the neocortex and their wiring diagrams poses a tremendous technical challenge but is key to mechanistically understanding complex cognitive functions, such as perception, memory, and decision-making. This study provides the most comprehensive wiring diagram of the adult neocortical microcircuit to date at the level of morphologically and electrophysiologically defined types of cells and reveals that neocortical micro-circuits are built from a small number of simple connectivity motifs that are recycled across the layers to generate the essential cortical connectivity structure. The finding that the complex functional cortical architecture can be broken down into a small number of connectivity motifs may lead to breakthroughs in our understanding of cortical computation at the circuit level. Given that numerous neuropsychiatric and neurological

diseases–such as autism spectrum disorders and epilepsy–may be associated with cell type-specific connectivity change in cortical microcircuits (18, 38, 39), such a detailed blueprint of cortical microcircuits could serve as an invaluable platform for screening and pinpointing specific circuit abnormalities in animal models of disease, thus providing a path to the development of comprehensive circuit-based, cell type-specific interventions that are otherwise not addressable with current treatments.

Supplementary Material

Refer to Web version on PubMed Central for supplementary material.

Acknowledgments

This work was supported by grants DP1EY023176 DP1OD008301 and R21EB016223 to A S T ; the McKnight Scholar Award to A S T ; the Arnold and Mabel Beckman Foundation Young Investigator Award to A S T ; P30EY002520 and T32EY07001; the Deutsche Forschungsgemeinschaft (DFG EXC 307) and the German Federal Ministry of Education and Research (BMBF; BCCN Tübingen FKZ 01GQ1002) CRC is supported by F30MH095440 T32GM007330 and T32EB006350 We thank P Saggau and J Reimer for help building the experiment rigs G Denfield for comments for the manuscript and D Yatsenko for help with data analysis The electrophysiological data presented in this manuscript are stored in the laboratory computers and tabulated in the main paper and in the supplementary materials The morphology of each neuron is preserved in the slices and many have been digitized and stored in the laboratory computers The data processing chain was assembled using the DataJoint library in MATLAB and Python (http://datajoint.github.com)

References and Notes

1. Markram H, et al. Interneurons of the neocortical inhibitory system. Nat Rev Neurosci. 2004; 5:793–807.10.1038/nrn1519 [PubMed: 15378039]
2. DeFelipe J, et al. New insights into the classification and nomenclature of cortical GABAergic interneurons. Nat Rev Neurosci. 2013; 14:202–216. [PubMed: 23385869]
3. Dumitriu D, Cossart R, Huang J, Yuste R. Correlation between axonal morphologies and synaptic input kinetics of interneurons from mouse visual cortex. Cereb Cortex. 2007; 17:81–91.10.1093/cercor/bhj126 [PubMed: 16467567]
4. Ascoli GA, et al. Petilla terminology: Nomenclature of features of GABAergic interneurons of the cerebral cortex. Nat Rev Neurosci. 2008; 9:557–568.10.1038/nrn2402 [PubMed: 18568015]
5. Jiang X, Wang G, Lee AJ, Stornetta RL, Zhu JJ. The organization of two new cortical interneuronal circuits. Nat Neurosci. 2013; 16:210–218.10.1038/nn.3305 [PubMed: 23313910]
6. Kepecs A, Fishell G. Interneuron cell types are fit to function. Nature. 2014; 505:318–326.10.1038/nature12983 [PubMed: 24429630]
7. Le Magueresse C, Monyer H. GABAergic interneurons shape the functional maturation of the cortex. Neuron. 2013; 77:388–405.10.1016/j.neuron.2013.01.011 [PubMed: 23395369]
8. Huang ZJ, Di Cristo G, Ango F. Development of GABA innervation in the cerebral and cerebellar cortices. Nat Rev Neurosci. 2007; 8:673–686.10.1038/nrn2188 [PubMed: 17704810]
9. Ting, J.; Daigle, T.; Chen, Q.; Feng, G. Patch-Clamp Methods and Protocols. Martina, M.; Taverna, S., editors. Vol. 1183. Springer; New York: 2014. p. 221-242.
10. Meyer HS, et al. Inhibitory interneurons in a cortical column form hot zones of inhibition in layers 2 and 5A. Proc Natl Acad Sci USA. 2011; 108:16807–16812.10.1073/pnas.1113648108 [PubMed: 21949377]
11. Jefferis GS, et al. Comprehensive maps of Drosophila higher olfactory centers: Spatially segregated fruit and pheromone representation. Cell. 2007; 128:1187–1203.10.1016/j.cell.2007.01.040 [PubMed: 17382886]
12. Hestrin S, Armstrong WE. Morphology and physiology of cortical neurons in layer I. J Neurosci. 1996; 16:5290–5300. [PubMed: 8757242]

13. Wang Y, et al. Anatomical, physiological and molecular properties of Martinotti cells in the somatosensory cortex of the juvenile rat. J Physiol. 2004; 561:65–90.10.1113/jphysiol.2004.073353 [PubMed: 15331670]
14. Gupta A, Wang Y, Markram H. Organizing principles for a diversity of GABAergic interneurons and synapses in the neocortex. Science. 2000; 287:273–278.10.1126/science.287.5451.273 [PubMed: 10634775]
15. Buchanan KA, et al. Target-specific expression of presynaptic NMDA receptors in neocortical microcircuits. Neuron. 2012; 75:451–466.10.1016/j.neuron.2012.06.017 [PubMed: 22884329]
16. Le Bon-Jego M, Yuste R. Persistently active, pacemaker-like neurons in neocortex. Front Neurosci. 2007; 1:123–129.10.3389/neuro.01.1.1.009.2007 [PubMed: 18982123]
17. Xiang Z, Prince DA. Heterogeneous actions of serotonin on interneurons in rat visual cortex. J Neurophysiol. 2003; 89:1278–1287.10.1152/jn.00533.2002 [PubMed: 12626611]
18. Chao HT, et al. Dysfunction in GABA signalling mediates autism-like stereotypies and Rett syndrome phenotypes. Nature. 2010; 468:263–269.10.1038/nature09582 [PubMed: 21068835]
19. Hu H, Cavendish JZ, Agmon A. Not all that glitters is gold: Off-target recombination in the somatostatin-IRES-Cre mouse line labels a subset of fast-spiking interneurons. Front Neural Circuits. 2013; 7:195.10.3389/fncir.2013.00195 [PubMed: 24339803]
20. Nassar M, et al. Diversity and overlap of paralbumin and somatostatin expressing interneurons in mouse presubiculum. Front Neural Circuits. 2015; 9:20.10.3389/fncir.2015.00020 [PubMed: 26005406]
21. Porter JT, et al. Properties of bipolar VIPergic interneurons and their excitation by pyramidal neurons in the rat neocortex. Eur J Neurosci. 1998; 10:3617–3628.10.1046/j.1460-9568.1998.00367.x [PubMed: 9875341]
22. Cauli B, et al. Molecular and physiological diversity of cortical nonpyramidal cells. J Neurosci. 1997; 17:3894–3906. [PubMed: 9133407]
23. Kawaguchi Y, Kubota Y. Physiological and morphological identification of somatostatin- or vasoactive intestinal polypeptide-containing cells among GABAergic cell subtypes in rat frontal cortex. J Neurosci. 1996; 16:2701–2715. [PubMed: 8786446]
24. Lee S, Hjerling-Leffler J, Zagha E, Fishell G, Rudy B. The largest group of superficial neocortical GABAergic interneurons expresses ionotropic serotonin receptors. J Neurosci. 2010; 30:16796–16808.10.1523/JNEUROSCI.1869-10.2010 [PubMed: 21159951]
25. Tamás G, Lorincz A, Simon A, Szabadics J. Identified sources and targets of slow inhibition in the neocortex. Science. 2003; 299:1902–1905.10.1126/science.1082053 [PubMed: 12649485]
26. Oláh S, et al. Regulation of cortical microcircuits by unitary GABA-mediated volume transmission. Nature. 2009; 461:1278–1281.10.1038/nature08503 [PubMed: 19865171]
27. Chittajallu R, Pelkey KA, McBain CJ. Neurogliaform cells dynamically regulate somatosensory integration via synapse-specific modulation. Nat Neurosci. 2013; 16:13–15.10.1038/nn.3284 [PubMed: 23222912]
28. Pfeffer CK, Xue M, He M, Huang ZJ, Scanziani M. Inhibition of inhibition in visual cortex: The logic of connections between molecularly distinct interneurons. Nat Neurosci. 2013; 16:1068–1076.10.1038/nn.3446 [PubMed: 23817549]
29. Lee S, Kruglikov I, Huang ZJ, Fishell G, Rudy B. A disinhibitory circuit mediates motor integration in the somatosensory cortex. Nat Neurosci. 2013; 16:1662–1670.10.1038/nn.3544 [PubMed: 24097044]
30. Pi HJ, et al. Cortical interneurons that specialize in disinhibitory control. Nature. 2013; 503:521–524.10.1038/nature12676 [PubMed: 24097352]
31. Taniguchi H, et al. A resource of Cre driver lines for genetic targeting of GABAergic neurons in cerebral cortex. Neuron. 2011; 71:995–1013.10.1016/j.neuron.2011.07.026 [PubMed: 21943598]
32. Reimer J, et al. Pupil fluctuations track fast switching of cortical states during quiet wakefulness. Neuron. 2014; 84:355–362.10.1016/j.neuron.2014.09.033 [PubMed: 25374359]
33. Wozny C, Williams SR. Specificity of synaptic connectivity between layer 1 inhibitory interneurons and layer 2/3 pyramidal neurons in the rat neocortex. Cereb Cortex. 2011; 21:1818–1826.10.1093/cercor/bhq257 [PubMed: 21220765]

34. De Marco García NV, Priya R, Tuncdemir SN, Fishell G, Karayannis T. Sensory inputs control the integration of neurogliaform interneurons into cortical circuits. Nat Neurosci. 2015; 18:393–401.10.1038/nn.3946 [PubMed: 25664912]

35. Xu X, Callaway EM. Laminar specificity of functional input to distinct types of inhibitory cortical neurons. J Neurosci. 2009; 29:70–85.10.1523/JNEUROSCI.4104-08.2009 [PubMed: 19129386]

36. Markram H, Lübke J, Frotscher M, Roth A, Sakmann B. Physiology and anatomy of synaptic connections between thick tufted pyramidal neurones in the developing rat neocortex. J Physiol. 1997; 500:409–440.10.1113/jphysiol.1997.sp022031 [PubMed: 9147328]

37. Perin R, Berger TK, Markram H. A synaptic organizing principle for cortical neuronal groups. Proc Natl Acad Sci USA. 2011; 108:5419–5424.10.1073/pnas.1016051108 [PubMed: 21383177]

38. Dajani DR, Uddin LQ. Local brain connectivity across development in autism spectrum disorder: A cross-sectional investigation. Autism Res. 2015; xxx:xxx.

39. Menuz K, Nicoll RA. Loss of inhibitory neuron AMPA receptors contributes to ataxia and epilepsy in stargazer mice. J Neurosci. 2008; 28:10599–10603.10.1523/JNEUROSCI.2732-08.2008 [PubMed: 18923036]

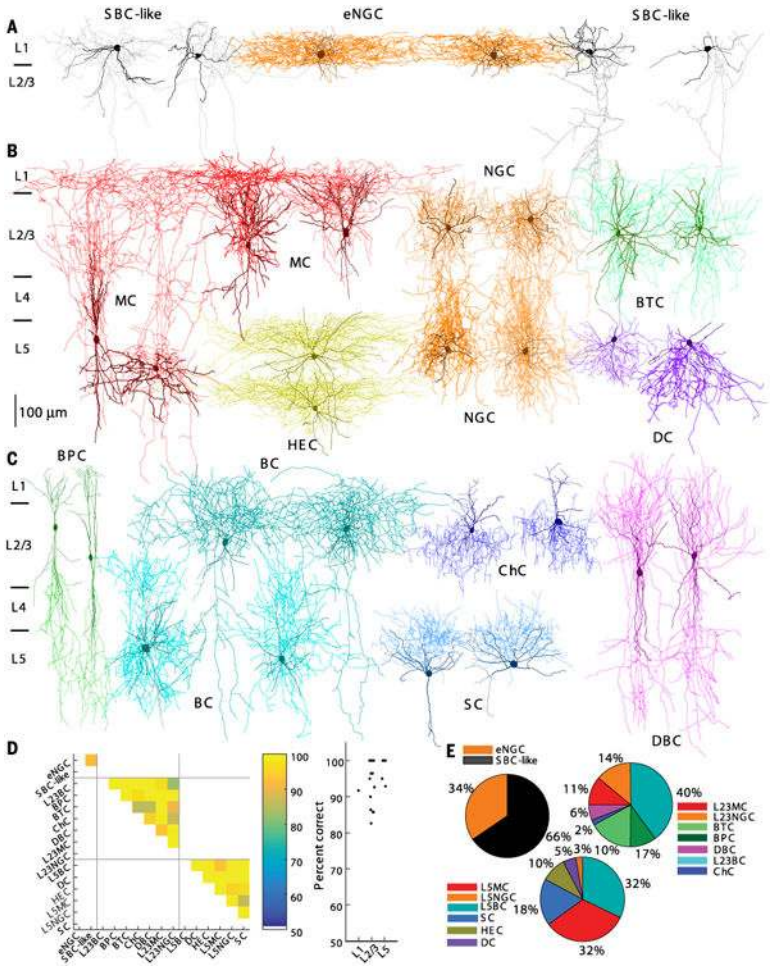

Fig. 1. Morphologically distinct GABAergic interneurons in L1, L23, and L5 of V1

(**A**) Two eNGCs (two middle; axon in dark orange and dendrite in brown) and four SBC-like cells. SBC-like cells on the left (two leftmost; axon in gray) have the axon arborizing mostly within layer 1, whereas SBC-like cells on the right (two rightmost; axon in gray) have the axon projecting mostly toward the deep layers. (**B**) Four MCs (both L23 and L5; axon in red and dendrite in dark red), four NGCs (L23 and L5; axon in orange and dendrite in brown), two HECs (axon in yellow and dendrite in dark yellow), two BTCs (axon in aquamarine and dendrite in green), and two DCs (axon in blue violet and dendrite in dark blue). (**C**) Two BPCs (axon in lime and dendrite in green), four BCs (both L23 and L5; axons in cyan and dendrite in dark cyan), two ChCs (axon in blue and dendrite in dark blue), two DBCs (axon in magenta and dendrite in purple), and two SCs (axon in dodge blue and dendrite in dark blue). (**D**) (Left) Cross-validated classification performance for each pair of cell types within a layer. (Right) Classification performance collapsed within each layer. (**E**) The proportion of each morphologically distinct type of interneurons.

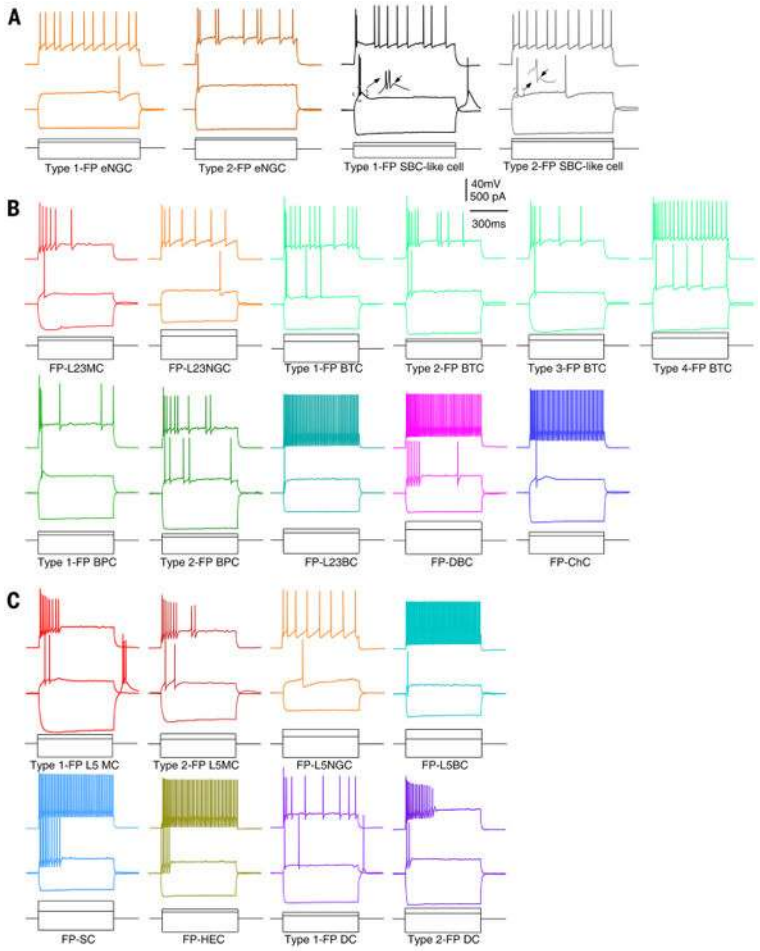

Fig. 2. Firing patterns (FPs) of morphologically distinct types of interneurons in V1

(**A**) Responses to hyperpolarizing, near-threshold, and suprathreshold current injections are shown for L1 eNGCs and SBC-like cells. The eNGCs had two types of firing patterns [LS, orange (leftmost); non-LS, dark orange], and SBC-like cells had two types of firing patterns (burst, black; no burst, gray). The eNGCs can be differentiated from SBC-like cells based on the absence of ADPs (see inset). (**B**) Responses to hyperpolarizing, near-threshold and suprathreshold current injections are shown for L23MCs, L23NGCs, BTCs, BPCs, L23BCs, DBCs, and ChCs. BTCs had four major types of firing patterns with subtle differences, and BPCs had two types of firing patterns that differ in the capability of burst. (**C**) Responses to hyperpolarizing, near-threshold, and suprathreshold current injections are shown for L5MCs, L5NGCs, L5BCs, SCs, HECs, and DCs. L5MCs and DCs had two types of firing patterns with subtle differences.The intrinsic membrane properties for each type of L1, L23, and L5 interneurons are presented in table S1.

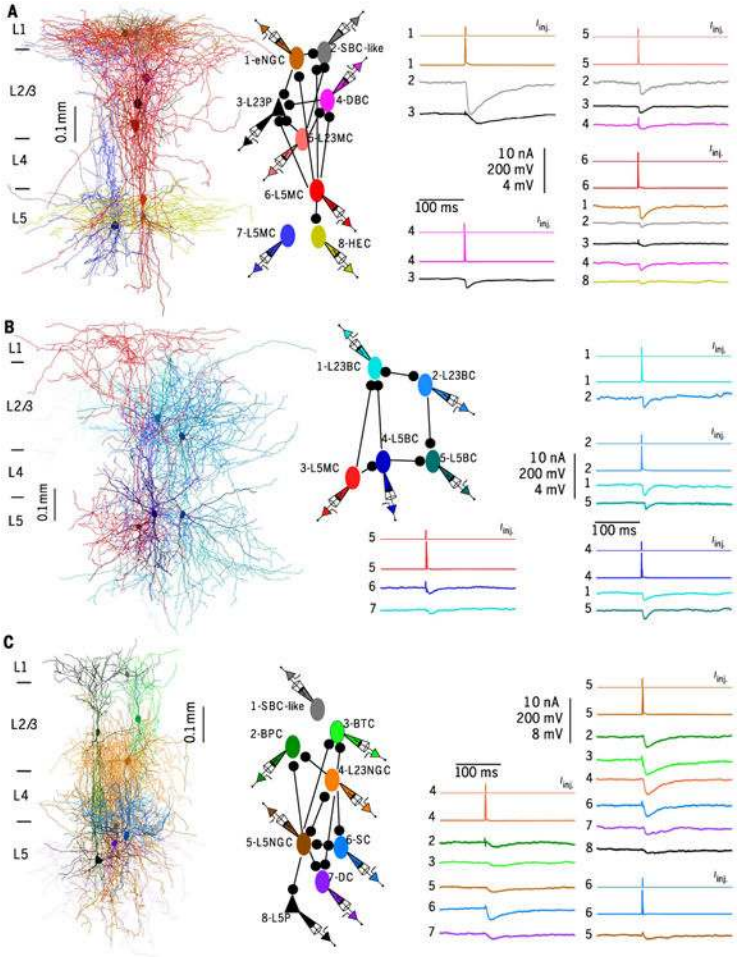

Fig. 3. Connections between morphologically distinct types of interneurons in V1

Right-most vertical scale bars from top to bottom show amplitudes of current injection ($I_{inj.}$ in nA), APs (mV), uIPSPs (mV). (**A**) (Left) Connections between eight simultaneously recorded neurons, including one eNGC, one SBClike cell, one DBC, one L23MC, one L23Pyr, one HEC, and two L5MCs. Each neuron was spatially separated in fig. S7A. (Middle) Connection diagram of the eight reconstructed neurons. (Right) APs elicited in presynaptic neurons and response traces of IPSPs evoked in postsynaptic neurons for each connection. (**B**) (Left) Connections between five simultaneously recorded neurons, including two L23BCs, two L5BCs, and one L5MC. Each neuron was spatially separated in fig. S7B. (Middle) Connection diagram of the five neurons. (Right) APs elicited in presynaptic neurons and response traces of IPSPs evoked in postsynaptic neurons for each connection. (**C**) (Left) Connections between eight simultaneously recorded neurons, including one SBC-like cell, one BPC, one BTC, one L23NGC, one L5Pyr, one L5NGC, one DC, and one SC. Each neuron was spatially separated in fig. S7C. (Middle) Connection diagram of the eight neurons. (Right) APs elicited in presynaptic neurons and response traces of IPSPs evoked in postsynaptic neurons for each connection.

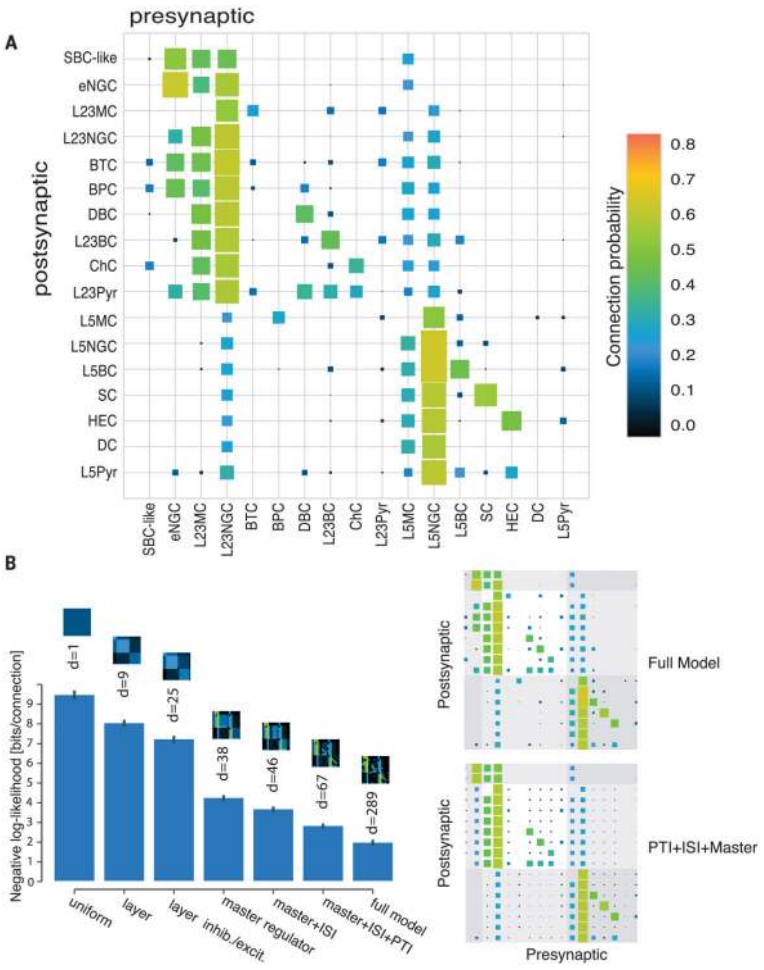

Fig. 4. Connectivity matrix for adult mouse V1

(**A**) Color-coded matrix showing the probability of finding a connected pair of neurons between two specific types within and across layers. For total connections found/total connections tested for each type of connection and the mean amplitude of the connections, see fig. S14, table S6, and the supplementary text. (**B**) A simple model incorporating three connectivity rules (master, ISI, and PTI) can explain most of the observed data. Bar height corresponds to the negative likelihood of the model per cell pair in bits, *d* denotes the degrees of freedom, and error bars show the standard deviation over 50 bootstrapped data sets. Models increase in complexity from left to right; pictograms on top of the bars show the corresponding connectivity matrix. The first four models assume that the connection probability is uniform, uniform within a layer, and uniform within a layer and excitatory/inhibitory neuron, respectively. The next three models include the connectivity rules. The full model has an individual connection probability for each type of connection. The Hinton plots on the right depict the connection probabilities according to the full model and the model including all three connectivity principles.

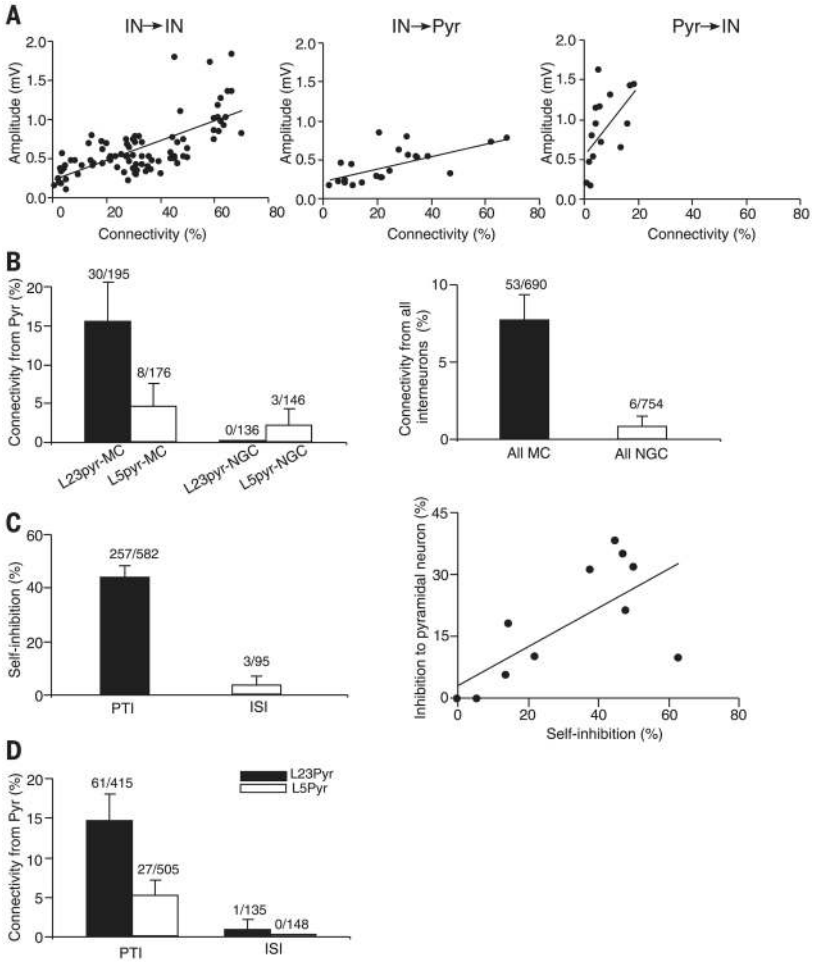

Fig. 5. Principles of connectivity in neocortical circuits

(**A**) Connection probability correlates with mean synaptic strength. Plot of the mean amplitudes of uIPSPs or uEPSPs of each type of connection against the connectivity rate for each type of connection [$r(96) = 0.70$, $P < 0.0001$ for interneuron→interneuron connection; $r(20) = 0.65$, $P = 0.001$ for interneuron→pyramidal neuron connection; $r(14) = 0.56$, $P = 0.03$ or pyramidal neuron→interneuron connection]. (**B**) (Left) Connectivity rate from excitatory cells to MCs and NGCs. (Right) Connectivity rate from all (non-MC, non-NGC) interneurons to MCs and NGCs. (**C**) (Left) The self-connections of PTI occurs in 44.2% (257/582; pooling across all PTIs), whereas self-inhibition between ISIs occurs only in 3.2% (3/95) of tested connections (GLM with factor of class of interneuron (PTI vs. ISI); $P < 0.0001$). (Right) There is a strong positive correlation between inhibition of pyramidal neurons and self-inhibition [$r(11) = 0.72$; $p = 0.01$]. Note that origin contains three points. (**D**) Pyramidal cells provided input to PTIs in 14.7% (61/415; pooling across all PTIs, from L23Pyr) and 5.3% (27/505, from L5Pyr) of the tested connections, whereas pyramidal cells rarely provided input to ISIs (0.74%, 1/135; 0.0%, 0/148 for L23 and L5 pyramidal neurons, respectively; GLM with factors of class of interneuron (PTI vs. ISI) and layer of pyramidal neuron; effect of interneuron class: $P = 0.005$; layer: $P = 0.009$; interaction: $P = 0.76$).

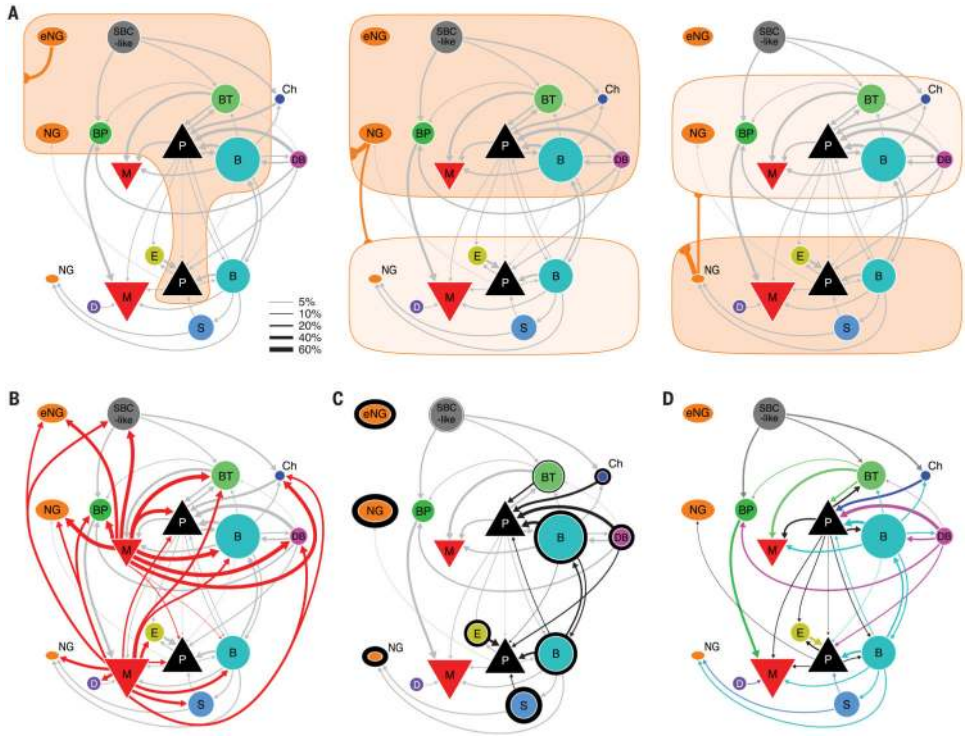

Fig. 6. Wiring diagram of V1 microcircuit

Different connectivity panels highlight different connectivity rules. Connectivity rates are indicated by line width (see legend). Connections with at least 5% connectivity rate are shown. Area of symbols indicate proportion of each cell type in the respective layer. Area of triangle depicting pyramidal cells does not represent proportion of pyramidal cells. (**A**) These diagrams illustrate volume transmission by eNGCs (left), L23NGCs (middle), and L5NGCs (right). The connections made by other neurons are shown in gray. (**B**) Connection of MCs to other cell types. (**C**) Self-inhibition is illustrated by the outline around each cell type (thickness illustrates the connectivity rate). Inhibition to pyramidal cells is highlighted in black. Connections from NGCs and MCs are omitted for clarity. (**D**) Connectivity between interneuron types and pyramidal cells is highlighted. Color of arrow is according to presynaptic cell type. Self-inhibition, volume transmission, and connections from MCs are omitted for clarity.